

Strotos, G., Malgarinos, I., Nikolopoulos, N. & Gavaises, M. (2016). Predicting the evaporation rate of stationary droplets with the VOF methodology for a wide range of ambient temperature conditions. *International Journal of Thermal Sciences*, 109, pp. 253-262. doi: 10.1016/j.ijthermalsci.2016.06.022



**CITY UNIVERSITY
LONDON**

[City Research Online](#)

Original citation: Strotos, G., Malgarinos, I., Nikolopoulos, N. & Gavaises, M. (2016). Predicting the evaporation rate of stationary droplets with the VOF methodology for a wide range of ambient temperature conditions. *International Journal of Thermal Sciences*, 109, pp. 253-262. doi: 10.1016/j.ijthermalsci.2016.06.022

Permanent City Research Online URL: <http://openaccess.city.ac.uk/15677/>

Copyright & reuse

City University London has developed City Research Online so that its users may access the research outputs of City University London's staff. Copyright © and Moral Rights for this paper are retained by the individual author(s) and/ or other copyright holders. All material in City Research Online is checked for eligibility for copyright before being made available in the live archive. URLs from City Research Online may be freely distributed and linked to from other web pages.

Versions of research

The version in City Research Online may differ from the final published version. Users are advised to check the Permanent City Research Online URL above for the status of the paper.

Enquiries

If you have any enquiries about any aspect of City Research Online, or if you wish to make contact with the author(s) of this paper, please email the team at publications@city.ac.uk.

1

2 **Predicting the evaporation rate of stationary droplets with the VOF**
3 **methodology for a wide range of ambient temperature conditions**

4

5 George Strotos^{1,a,*}, Ilias Malgarinos^{1,b}, Nikos Nikolopoulos^{1,c}, Manolis Gavaises^{1,d}

6 ¹School of Engineering and Mathematical Sciences, City University London, Northampton
7 Square, EC1V 0HB, London, UK

8 ^a George.Strotos.1@city.ac.uk

9 ^b Ilias.Malgarinos.1@city.ac.uk

10 ^c Nikolaos.Nikolopoulos.1@city.ac.uk

11 ^d M.Gavaises@city.ac.uk

12 *Corresponding author

13

14 **Abstract**

15 This paper presents CFD predictions for the evaporation of nearly spherical suspended droplets
16 for ambient temperatures in the range 0.56 up to 1.62 of the critical fuel temperature, under
17 atmospheric pressures. The model solves the Navier-Stokes equations along with the energy
18 conservation equation and the species transport equations; the Volume of Fluid (VOF)
19 methodology has been utilized to capture the liquid-gas interface using an adaptive local grid
20 refinement technique aiming to minimize the computational cost and achieve high resolution at
21 the liquid-gas interface region. A local evaporation rate model independent of the interface
22 shape is further utilized by using the local vapor concentration gradient on the droplet-gas
23 interface and assuming saturation thermodynamic conditions. The model results are compared
24 against experimental data for suspended droplet evaporation at ambient air cross flow including
25 single- and multi-component droplets as well as experiments for non-convective conditions. It is
26 proved that the detailed evaporation process under atmospheric pressure conditions can be
27 accurately predicted for the wide range of ambient temperature conditions investigated.

28

29 **Keywords:** VOF, evaporation, multi-component, high temperature

31 1 INTRODUCTION

32 Droplet evaporation is an important phenomenon realized in several engineering and physical
33 processes; it has been addressed in several textbooks, see selectively [1-4] and review articles
34 [5-8]. Numerical modelling of droplet evaporation started with the idealized evaporation of a
35 spherical, isolated, motionless and constant temperature droplet in an inert gas environment.
36 Under these assumptions, Godsave [9] and Spalding [10] derived the widely known “ d^2 -law”
37 which predicts that the squared diameter of the droplet reduces linearly with time. Following
38 this approach, these strict assumptions were relaxed by taking into consideration the relative
39 velocity between the air and the droplet, the transient droplet heating, the Stefan flow effects,
40 the evaporation of multicomponent droplets and other secondary phenomena. The transient
41 droplet heating was accounted with the Infinite Conductivity Model (ICM) [11] and the spatial
42 temperature distribution inside the droplet with the Finite Conductivity Model (FCM) [12], the
43 Effective Conductivity Model (ECM) [13] and the parabolic temperature profile model [14].
44 Regarding the Stefan flow effects which arise from the radial vapor motion, the models of
45 Abramzon & Sirignano [13] and Yao et al. [15] are widely used, while there is a large variety of
46 available heat/mass transfer correlations to account for the relative droplet-gas motion [7]. The
47 performance of the aforementioned models was assessed in comparative studies such as in [16-
48 19].

49 Modelling of multicomponent droplet evaporation has been also a challenging task since most
50 of the fuels are mixtures of many hydrocarbon components. For a bi-component mixture, the
51 preferential evaporation behavior obeys the distillation behavior of the two components, in
52 which the most volatile species evaporates first followed by the vaporization of the less volatile
53 component. The properties of the mixture depend, in addition to the local temperature, to the
54 concentration. Thus, additional equations need to be solved, accounting for the variation of the
55 species concentration in the liquid phase. Similar to the modelling of the thermal behavior of the
56 droplet, the temporal evolution of the species concentration is simulated by using 0-D or 1-D
57 models, usually known as the Infinite Diffusivity Models (IDM) [20-22] and the Finite
58 Diffusivity Models (FDM) [23-26], respectively.

59 The aforementioned simplified approaches are suitable for Lagrangian spray models predicting
60 the evolution of sprays plumes in combustion systems, comprised by a large number of
61 polydispersed size droplets, as they do not require a lot of computational resources. On the other
62 hand, their applicability is limited to spherical or near spherical droplets; moreover, they cannot
63 give insight of the complex 3-D fluid and thermal transport processes taking place during

64 evaporation. Such models require solution of the Navier-Stokes equations along with the energy
65 and species transport equations both for the liquid and gaseous phases simultaneously. The
66 earliest CFD works on droplet evaporation were those of [27-29] who examined the evaporation
67 of single-component spherical droplets and derived useful correlations for the Nusselt and
68 Sherwood numbers, followed later by [30-34]. These works have revealed the importance of the
69 spatial distribution of the velocity, temperature and vapor concentration field and they can be
70 considered as benchmark cases for the validation of 0-D and 1-D models. Later, they were
71 extended to multicomponent fuels in [35-38] and to high pressure conditions in [39]. A common
72 feature of the aforementioned CFD works is that they use a grid fitted to the liquid-gas
73 interface; this provides an accurate representation of the flow field and allows for the
74 determination of the local momentum-heat-mass transfer rates, but they are limited to 2D
75 axisymmetric flows with no or low surface deformation as in [40]. On the other hand, the
76 Volume of Fluid (VOF) and Level Set (LS) methodologies among others can capture the 3D
77 droplet deformation (and even breakup), but with a less accurate prediction of the flow field at
78 the interface region. Recent works on droplet evaporation with the VOF methodology include
79 those of [41-44]. In these works a local evaporation model was used; Schlottke & Weigand [41]
80 used a virtual mass averaged velocity to calculate the source term of the continuity equation at
81 the interface region which improved the model performance. Furthermore, Strotos et al. [42]
82 and Banerjee [43] performed parametric studies for bi-component droplet evaporation while
83 Ghata & Shaw [44] studied the vaporization of fiber-supported droplets and included the effect
84 of thermocapillary stresses at the interface.

85 The present work examines the droplet evaporation using the solution of the Navier-Stokes
86 equations along with the energy conservation equation, the transport of species and the VOF
87 methodology for tracking the droplet interphase. The validation study examines single- and
88 multi-component droplets for a wide range of ambient temperature conditions under
89 atmospheric pressure. Relative to previous relevant CFD studies with the VOF methodology
90 resolving the complete fluid transport processes during vaporization, including the work of the
91 authors presented in [42], this is one of the first studies (at least to the authors' knowledge) that
92 examines droplet evaporation at temperature ambient conditions above the critical fuel
93 temperature and validates against experimental data the model for a wide range of temperatures.
94 The following sections include the description of the numerical model, the cases simulated,
95 followed by the model predictions for low and high ambient temperature conditions. The
96 conclusions of this work are summarized at the end.

97

98 2 MATHEMATICAL MODEL

99 2.1 Flow field equations

100 The numerical model involves the solution of the Navier-Stokes equations along with the
 101 solution of the transport equation of the liquid phase. The model is an extension of the one used
 102 in [45-47] including phase change. In addition, the numerical model employs the Volume of
 103 Fluid (VOF) methodology [48] for capturing the droplet liquid-gas interphase. In this
 104 methodology, the liquid phase is identified by the liquid volume fraction a_l (defined as the
 105 liquid volume in a cell divided by the cell volume) and its transport is given by:

$$106 \quad \frac{1}{\rho_l} \left[\frac{\partial(a_l \rho_l)}{\partial t} + \nabla \cdot (a_l \rho_l \vec{u}) \right] = - \sum_{k=1}^{N_{sp}} \dot{m}''''_{evap,k} \quad (1)$$

107 where ρ_l is the liquid phase density, \vec{u} is the velocity vector and $\dot{m}''''_{evap,k}$ (kg/s/m³) is the
 108 volumetric evaporation rate each of the N_{sp} species composing the liquid phase. The equation
 109 (1) can be used for an arbitrary number of phases N_{ph} (here $N_{ph}=2$), while the corresponding
 110 volume fraction of the gaseous phase can be obtained from the equality $a_g=1-a_l$. The momentum
 111 equations for both phases are written in the form:

$$112 \quad \frac{\partial(\rho \vec{u})}{\partial t} + \nabla \cdot (\rho \vec{u} \vec{u}) = -\nabla p + \nabla \cdot [\mu(\nabla \vec{u} + \nabla \vec{u}^T)] + \rho \vec{g} + \vec{F}_{vol} \quad (2)$$

113 where \vec{F}_{vol} is the volumetric force due to surface tension. This is calculated based on the
 114 Continuum Surface Force (CSF) approach of Brackbill et al. [49] and it is equal to:

$$115 \quad \vec{F}_{vol} = \sigma \kappa \vec{n} \frac{\rho}{\frac{1}{2}(\rho_l + \rho_g)} \quad , \quad \vec{n} = \nabla a \quad , \quad \kappa = -\nabla \cdot \left(\frac{\vec{n}}{|\vec{n}|} \right) \quad (3)$$

116 where σ is the surface tension coefficient, \vec{n} is the normal vector at the interface and κ is the
 117 curvature of the interface. Alternatively, the surface tension forces can be included in the
 118 momentum equations by using the Continuum Surface Stress (CSS) model by Lafaurie et al.
 119 [50] which inherently includes the effects of the variation of the surface tension coefficient
 120 along the interface. Equation (4) represents the CSS model, where \mathbf{I} is the unit tensor and \otimes is
 121 the tensor product of two vectors.

$$122 \quad \vec{F}_{vol} = \nabla \cdot \left[\sigma \left(|\vec{n}| \mathbf{I} - \frac{\vec{n} \otimes \vec{n}}{|\vec{n}|} \right) \right] \quad , \quad \vec{n} = \nabla a \quad (4)$$

123

124 Additionally, the transport equations for energy, vapor and liquid species concentration are
 125 solved:

126
$$\frac{\partial(\rho E)}{\partial t} + \nabla \cdot [\vec{u}(\rho E + p)] = \nabla \cdot [k\nabla T - \sum_{q=1}^{Nph} (a_q \sum_{k=1}^{Nsp} h_{q,k} \vec{J}_{q,k})] - \sum_{k=1}^{Nsp} \dot{m}_{evap,k}''' L_k \quad (5)$$

127
$$\frac{\partial(a_q \rho_q Y_{q,k})}{\partial t} + \nabla \cdot (a_q \rho_q Y_{q,k} \vec{u}) = \nabla \cdot (-a_q \vec{J}_{q,k}) + S_{Y,q} \quad (6)$$

128
$$\vec{J}_{q,k} = -\rho_q D_{q,k,m} \nabla Y_{q,k} \quad , q=\text{gas or liquid} \quad (7)$$

129 where $\vec{J}_{q,k}$ is the dilute approximation of the diffusion flux of species k at the mixture of phase
 130 q (neglecting the Soret effect), $D_{q,k,m}$ is the diffusion coefficient of kth species in the mixture of
 131 phase q (either gas or liquid). Equation (6) is solved in the gas phase (q=gas) for all the vapor
 132 species (k=1÷Nsp) with a source term equal to $S_{Y,q} = \dot{m}_{evap,k}'''$. For the case of multicomponent
 133 droplets, the same equation is also solved in the liquid phase (q=liquid) for all liquid species
 134 with a source term equal to $S_{Y,q} = -\dot{m}_{evap,k}'''$, except of the main liquid species (k=Nsp), since
 135 its concentration can be computed from the summation of the liquid species concentrations,
 136 which must equal to one.

137 The properties of the pure components are assumed to be a function of temperature according to
 138 [51, 52] and they are updated at every iteration during the numerical solution. The mixture
 139 properties (either in the gas or the liquid phase for the case of multicomponent evaporation)
 140 follow a mass average rule based on the concentration, while the gas phase density is obtained
 141 by assuming incompressible ideal gas.

142 The numerical settings used for the simulations are: Laminar flow, explicit VOF solution with
 143 the Geometric reconstruction scheme [53], Second Order Upwind (SOU) discretization [54] for
 144 the momentum and energy equations, First Order Upwind (FOU) for the species transport
 145 equations, Body Force Weighted (BFW) pressure interpolation scheme [55], pressure-velocity
 146 coupling with the PISO algorithm [56], variable timestep with Courant number $C=0.25$ both for
 147 the interface tracking and the whole computational domain (global Courant number).

148 The commercial CFD code ANSYS FLUENT v14.5 [55] has been utilized for the solution of
 149 the flow equations with a number of user defined functions (UDF) for resolving the above
 150 processes; more specifically, UDFs have been used for applying the automatic local grid
 151 refinement technique and the interface sharpening algorithm [47] required to minimize the
 152 interface diffusion which is promoted by the evaporation source terms. Moreover, the
 153 evaporation rate model described in the next section is also implemented using UDF together
 154 with the functions addressing the fluid, vapor and gas properties as function of local temperature
 155 [51, 52].

156

157 2.2 Evaporation rate model

158 The evaporation rate is calculated as in [42, 43, 57, 58] by applying the simplified Fick's law at
 159 the liquid-gas interface cells:

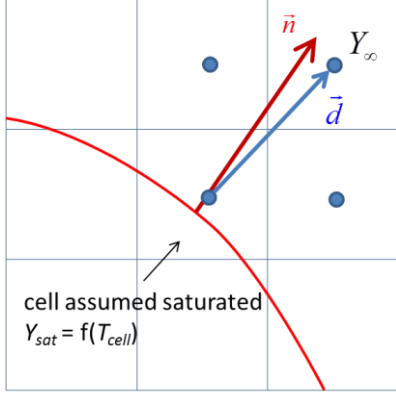
$$160 \quad \dot{m}''_{evap,k} = \rho_g D_{g,k,m} \left(\frac{dY_{g,k}}{dn} \right)_{surf}, \quad k=1 \div N_{sp} \quad (8)$$

161 The evaporation source term $\dot{m}'''_{evap,k}$ is obtained by multiplying equation (8) with
 162 $A_{l,cell}/V_{cell} = |\nabla a|$. The evaporation rate of equation (8) is independent of the interface shape
 163 and does not require any reference length or velocity. Although it is based on a diffusion law,
 164 the flow conditions are taken into account through the solution of the Navier-Stokes equations
 165 which advect the vapor and modify the local concentration gradient. Besides this simplified
 166 Fick's law, a more physically correct expression was also examined which takes into
 167 consideration the Stefan flow:

$$168 \quad \dot{m}''_{evap,k} = \frac{\rho_g D_{g,k,m} \left(\frac{dY_{g,k}}{dn} \right)_{surf}}{1 - Y_{g,k,sat}} \quad (9)$$

169 Equation (9) has been used in Schlottke & Weigand [41] among others and it is valid only for
 170 single-component evaporation. For multi-component evaporation, the exact expression for the
 171 evaporation rate was given in Renksizbulut & Bussmann [38] but it was not examined here
 172 since it is more complicated and computationally expensive. For low evaporation rates and
 173 when the droplet temperature is not close to the boiling temperature (i.e. small Spalding
 174 numbers, $B_M \ll 1$), both expressions are valid.

175 The key parameter in the implementation of the evaporation rate model is the calculation of the
 176 concentration gradient magnitude $(dY_g/dn)_{surf}$. The interfacial cells are assumed to be saturated
 177 and the vapor saturation concentration Y_{sat} is calculated as a function of the cell temperature
 178 (and liquid composition when multicomponent evaporation is examined). An algorithm is used
 179 to identify the closest neighbor cell (subscript ∞) to the direction of the normal vector of the
 180 interface \vec{n} ; this is illustrated in Fig. 1. Denoting as \vec{d} the vector connecting the two cells, two
 181 options exist for the calculation of the concentration gradient (see details in Fig. 1) in non-
 182 orthogonal unstructured grids. The first one is the simplest but less accurate when the vectors \vec{n}
 183 and \vec{d} are not aligned. The second one is more accurate since it accounts for the angle between
 184 the two vectors; it works for all types of grid and it is the default method in the present model.



$$1. \left(\frac{dY_g}{dn} \right)_{surf} = \frac{Y_{sat} - Y_{\infty}}{|\vec{d}|}$$

$$2. \left(\frac{dY_g}{dn} \right)_{surf} = \frac{Y_{sat} - Y_{\infty}}{|\vec{d}|} \frac{\vec{d}}{|\vec{d}|} \cdot \frac{\vec{n}}{|\vec{n}|}$$

185

186 Fig. 1: Illustration of the two different methods employed for the estimation of the vapor
 187 concentration gradient at the liquid-gas interface. The 2nd method has been finally adopted in the
 188 present work.
 189

190 Finally, the vapor diffusion coefficient $D_{g,k,m}$ of the k^{th} species in the gas mixture, is obtained
 191 by using the dilute approximation (Eq. 10), in which $X_{g,k}$ is the mole fraction of species k in the
 192 gas phase and $D_{g,i,j}$ is the binary diffusion coefficient of species i in species j ; the latter is a
 193 function of temperature:

$$194 \quad D_{g,k,m} = \frac{1 - X_{g,k}}{\sum_{j,j \neq i} (X_{g,j} / D_{g,i,j})} \quad (10)$$

195

196 3 DESCRIPTION OF THE TEST CASES SIMULATED

197 The mathematical model used is validated against 3 sets of experimental data for suspended droplet
 198 evaporation for: (a) convective air flow conditions (experimental data of Daïf et al. [59]), (b) the
 199 data of Wong & Lin [60] and (c) under microgravity conditions in a quiescent gas environment
 200 (experimental data of Nomura et al. [61]). The cases examined are presented in Table 1; they all
 201 refer to atmospheric ambient pressure. As it can be seen, they cover a wide range of conditions
 202 including single- and multi-component evaporation, sub- and super-critical gas temperature
 203 conditions, low and moderate Re numbers, as also species with a large volatility difference (n-
 204 heptane and n-decane). More specifically, cases 1-3 correspond to the experimental data of Daïf
 205 et al. [59] who examined droplet evaporation at low temperature conditions and moderate Re

206 numbers for droplets consisting of n-heptane (case 1), n-decane (case 2) and a mixture of the
 207 two with 74% n-heptane (case 3). Case 4 corresponds to the experimental data of Wong & Lin
 208 [60] who examined the evaporation of n-decane droplets in a high temperature gas environment
 209 and low Re number flow. Cases 5-8 correspond to the experimental data of Nomura et al. [61],
 210 who investigated suspended n-heptane droplets in high temperature ambient conditions. Each
 211 set of the aforementioned experimental data is examined in a separate section in the present
 212 paper, in which the experimental and the numerical setup are presented in detail.

213

214 Table 1: Experimental conditions examined

215

case	species	d_0 [mm]	$T_{d,0}$ [K]	T_∞ [K]	u_∞ [m/s]	Re_0	ref
1	C7	1.052	300	356	3.20	159	[59]
2	C10	1.386	315	348	3.10	210	[59]
3	C7-C10 74-26%	1.334	294	348	3.10	203	[59]
4	C10	1.961	315	1000	1.0	17	[60]
5	C7	0.700	300	471	~ 0	~ 0	[61]
6	C7	0.700	300	555	~ 0	~ 0	[61]
7	C7	0.700	300	648	~ 0	~ 0	[61]
8	C7	0.700	300	741	~ 0	~ 0	[61]

216

217

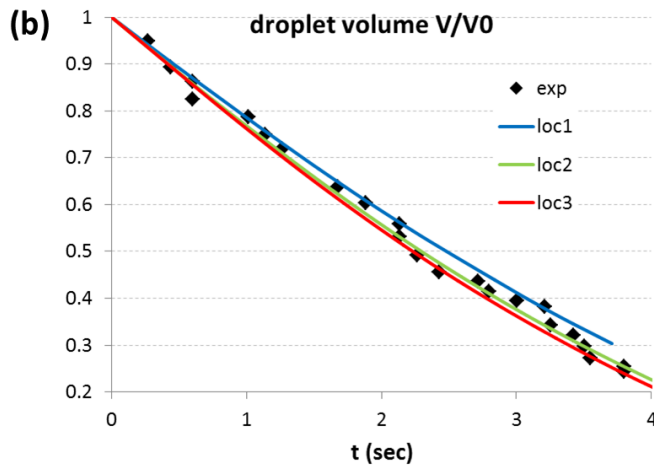
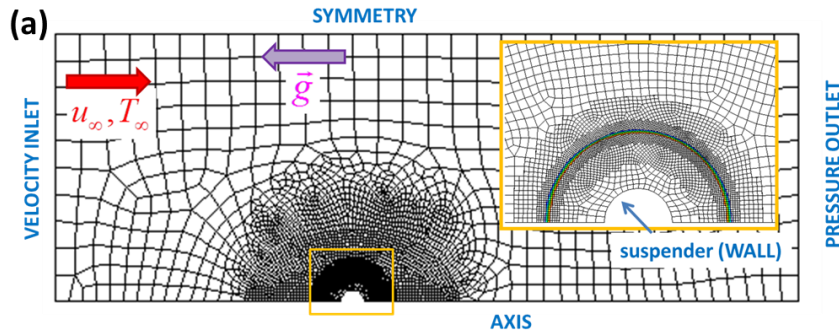
218 **4 RESULTS & DISCUSSION**

219 **4.1 Evaporation at low temperature conditions. Experimental data of Daïf et al.**
220 **[59]**

221 In this section the numerical model is validated against the experimental data reported in Daïf et
222 al. [59] for cases 1-3 of Table 1. These refer to subcritical ambient temperature conditions and
223 include the evaporation of single- and multicomponent droplets at moderate Re numbers. In [59]
224 the droplets were held in suspension at the spherical head of a capillary tube (400 and 200 μ m
225 respectively), which was placed perpendicularly to the gas flow. They used a video camera to
226 record the droplet diameter and an infrared thermo-graphic system to measure the droplet's
227 surface temperature.

228 The computational domain, the boundary conditions and the grid used for these cases are shown
229 in Fig. 2a; they are similar to these used in Strotos et al. [42]. The flow was assumed to be 2D-
230 axisymmetric since the Re number is below 400 for all cases examined and the presence of the
231 capillary tube is not expected to induce 3D effects. The spherical head of the suspender was
232 assumed to be an adiabatic impermeable wall and the liquid contact angle was set to 10 degrees
233 as in [42]. Regarding the initial conditions, uniform velocity, temperature and concentration
234 fields were assumed. The grid used is unstructured with 2 levels of adaptive local refinement;
235 this is based on the work of Theodorakakos & Bergeles [62] and implemented here as in
236 Malgarinos et al. [45]. A grid independent solution is achieved by using 2 levels of local grid
237 refinement as shown in Fig. 2b for the prediction of the dimensionless droplet volume temporal
238 evolution. This is a good compromise between accuracy and computational cost which is
239 approximately 1.7CPU-days for each second of physical time for the single-component cases
240 and 2.3CPU-days/sec for the bi-component evaporation case.

241

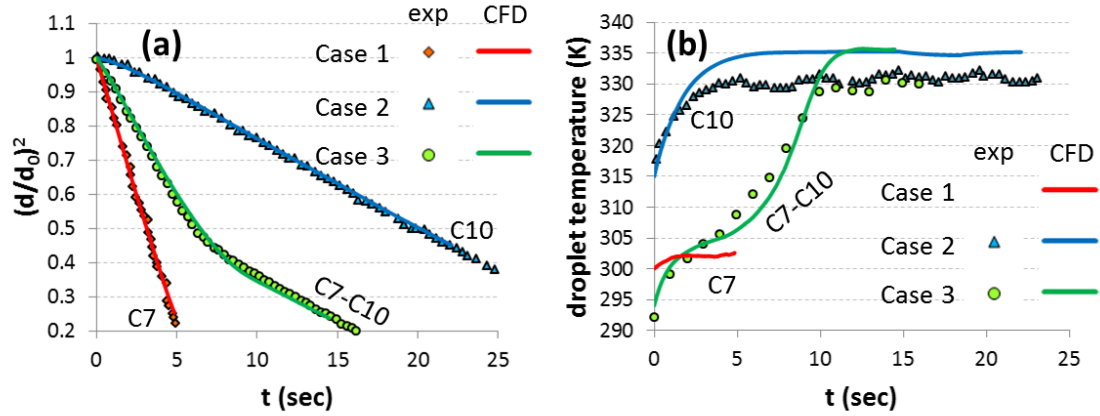


242

243 Fig. 2: (a) Computational domain and boundary conditions employed. The inset figure shows
 244 the grid topology around the liquid-gas interface for two levels of adaptive local grid
 245 refinement. (b) Temporal evolution of droplet's non-dimensional volume for the case 1 using
 246 one-, two- and three-levels of local grid refinement.
 247

248 The temporal evolution of the non-dimensional droplet squared diameter and the mean droplet
 249 temperature for the cases of Daïf et al. [59] are presented in Fig. 3a and Fig. 3b, respectively.
 250 The predictions are in good agreement with the experimental data regarding the droplet size,
 251 while the wet-bulb temperature of n-decane is overestimated by 4°C; this is within the accuracy
 252 of previously published studies for the same case [25, 42, 63, 64]. Single-component droplets
 253 (cases 1 and 2) after an initial heat-up period follow the d^2 -law and they reach the wet-bulb
 254 temperature corresponding to the experimental conditions. The two-component droplet (case 3)
 255 exhibits preferential evaporation in which the more volatile n-heptane evaporates first and then
 256 the less volatile n-decane follows. The relevant physical processes during the multicomponent
 257 evaporation have been discussed in depth discussed in Strotos et al. [42, 65].

258

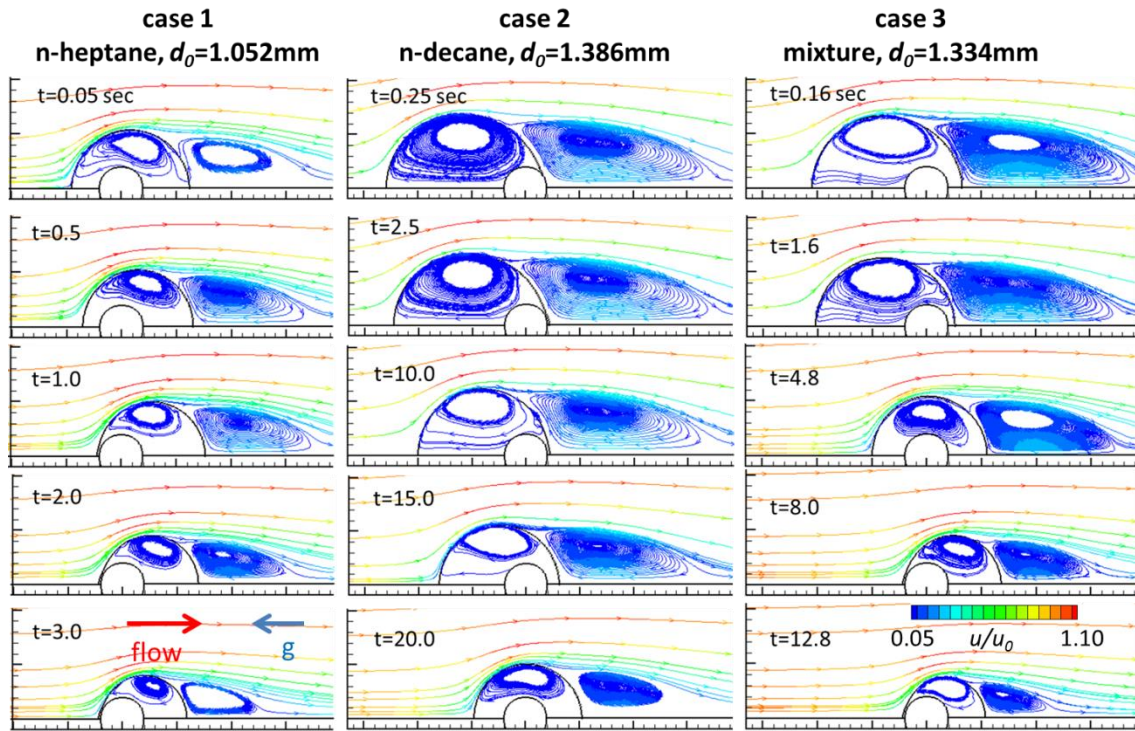


259

260 Fig. 3: Model predictions for the experimental data of Daif et al. [59]. Temporal evolution of (a)
 261 droplet size and (b) mean droplet temperature. No experimental data were provided for the
 262 droplet temperature in case 1.
 263

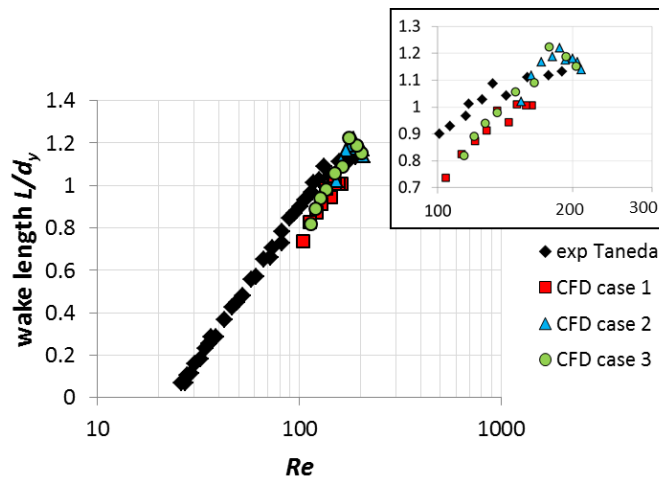
264 Initially, the spherical suspender lies at the centre of the droplet; under the action of
 265 gravitational and aerodynamic forces the droplet moves either upwards or downwards as shown
 266 in Fig. 4. The n-heptane droplet (case 1) is relatively light and moves upwards (opposite to the
 267 direction of gravity in Fig. 4), while the droplets of the other two cases are heavier and they
 268 move initially downwards (in the direction of gravity in Fig. 4). As the droplet evaporates and
 269 becomes lighter, the gravitational force become smaller compared to the aerodynamic one and
 270 the droplet progressively moves to the other side of the suspender. After reaching an
 271 equilibrium position, the droplets are held in touch with the suspender due to the adhesion
 272 forces. Behind the droplet, a large recirculation zone appears and its length is plotted versus the
 273 gas phase Re number in Fig. 5; the experimental data of Taneda [66] for a solid sphere are also
 274 shown. The wake length increases with increasing Re number and it is slightly restricted
 275 compared to the one formed under the same flow conditions behind a solid sphere. This is
 276 attributed to the liquid phase recirculation which moves the flow separation point towards the
 277 rear of the droplet and suppresses the length of the wake, as also reported previously in
 278 Sirignano [2].

279



280

281 Fig. 4: Predicted transient droplet motion and flow field streamlines for the experiments of Daïf
 282 et al. [59] (cases 1-3).
 283



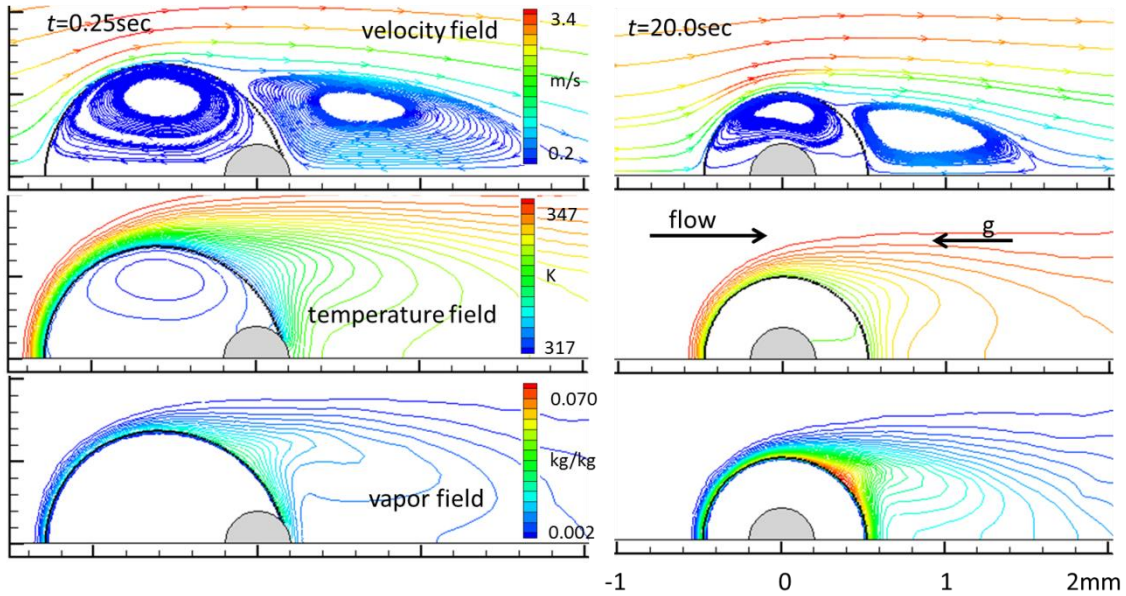
284

285 Fig. 5: Dependence of the wake recirculation length with the Re number for cases 1-3.
 286

287 In Fig. 6 representative velocity, temperature and vapor fields are presented for the n-decane
 288 case at 0.25 and 20.0sec; the velocity field is depicted by the streamlines colored with the
 289 velocity magnitude. The spatial distribution of the temperature and the vapor field is influenced
 290 by the recirculation zones formed inside and behind the droplet, as also the presence of the solid
 291 suspender. Inside the droplet, a relatively cooler region is identified at the vortex core (as also

292 observed in [29, 30]), while at the wake behind the droplet the temperature and the vapor
 293 concentration fields are similar between them and they are influenced by the gas phase vortex.

294



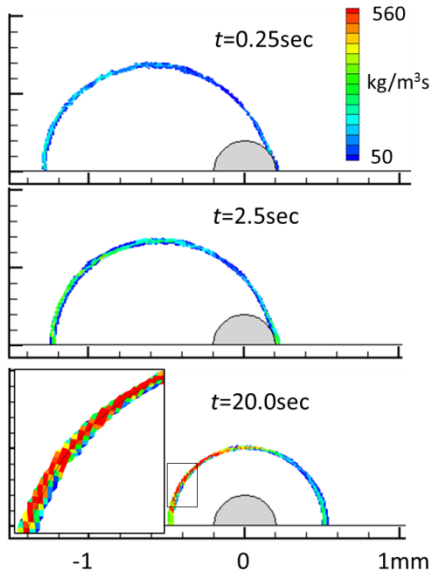
295

296 Fig. 6: Velocity streamlines, temperature and vapor concentration field for the n-decane droplet
 297 (case 2).

298

299 In Fig. 7 the spatial distribution of the evaporation source term (in $\text{kg/m}^3\text{s}$) at selected time
 300 instances is presented for the n-decane droplet; the non-interpolated contours shown correspond
 301 to the region between VOF values equal to 0.01 and 0.99. As it can be seen, there is a narrow
 302 region at the interface (2-3 cells) in which the evaporation source term is distributed and it
 303 maximizes near the 0.5 iso-VOF line, in which the quantity $|\nabla a|$ maximizes too (see also the
 304 inset figure at $t=20\text{sec}$). The thickness of this region in length units depends on the grid density,
 305 but it has a minor effect on the overall evaporation process, as shown in Fig. 2b. The
 306 evaporation rate increases with time, since the droplet temperature also increases; it is
 307 interesting to observe that the maximum evaporation rate is observed around $30\text{-}40^\circ$ away from
 308 the front stagnation point, which was also observed in Shih & Megaridis [31]. The minimum
 309 evaporation rate is observed near the point of flow separation at approximately $130\text{-}140^\circ$; this
 310 behavior was also observed in Haywood et al. [28]. The spatial distribution of the evaporation
 311 rate is not smooth and this is ought to the imperfect distribution of the VOF values over the
 312 computational cells.

313



314

315 Fig. 7: Spatial distribution of the evaporation rate at different time instances for the n-decane
 316 droplet (case 2).
 317

318 One of the parameters examined was the effect of the thermo-capillary flow (Marangoni effect)
 319 induced by the variation of the surface tension coefficient along the interface. This is achieved
 320 by using the CSS formulation [50] instead of the CSF model [49] in order to calculate the
 321 surface tension forces in the momentum equations. As it was also shown in Strotos et al. [42],
 322 the temperature along the interface does not exhibit large variations and the Marangoni effect
 323 does not affect the droplet evaporation for these specific cases. On the other hand, it seems to
 324 create a kind of unsteadiness by increasing the fluctuations of the droplet shape but without a
 325 noticeable effect on the liquid phase internal circulation; unsteadiness in thermo-capillary flows
 326 were also observed in Shih & Megaridis [32]. The single-component cases 1-2 were also
 327 examined by using the evaporation rate of equation (9). The results have shown that it has a
 328 negligible effect on the prediction of the phenomenon due to the low evaporation rate and thus it
 329 is not presented.

330

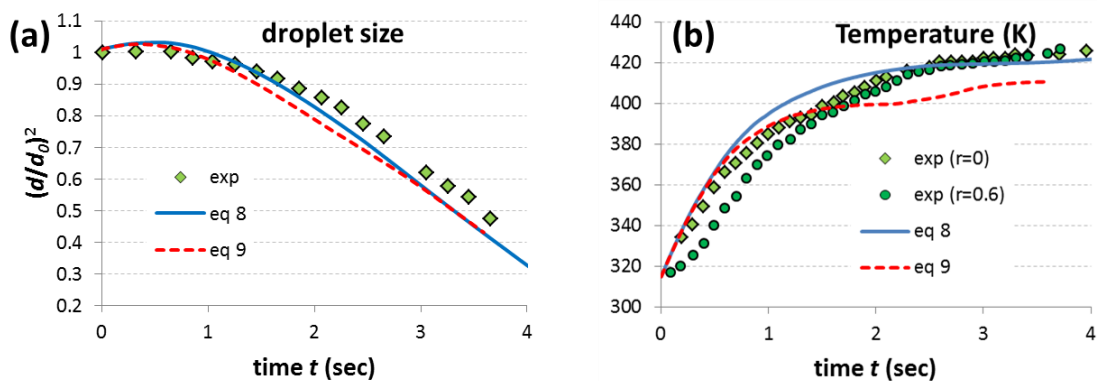
331 **4.2 Evaporation at high temperature conditions. Experimental data of Wong &** 332 **Lin [60]**

333 The 4th case of Table 1 corresponds to the experimental data of Wong & Lin [60] who examined
 334 the evaporation of n-decane droplets in a supercritical gas environment ($T_\infty= 1000\text{K}$,
 335 $T_{cr,C7}=617.7\text{K}$). The droplet was suspended at a ceramic shell attached to a $100\mu\text{m}$ glass
 336 filament; the droplet internal temperature distribution was measured by using thermocouples
 337 ($25\mu\text{m}$ wire diameter and $\sim 70\mu\text{m}$ bead diameter) placed at different positions inside the droplet.

338 This set of experimental data has been widely used in validation studies for 0-D and 1-D models
 339 [16, 19, 63, 67, 68] as also in CFD studies by [30, 33], which assumed a spherical droplet shape
 340 and neglected the presence of the shell-like suspender. In the present study the presence of the
 341 suspender has been considered but assumed to be spherical since its exact geometry and
 342 dimensions were not reported in the relevant paper.

343 The model predictions for the droplet size and the mean droplet temperature are shown in Fig. 8
 344 by using the two variations of the evaporation model described in section 2.2, i.e using equation
 345 (8) and (9), respectively. The predictions for the droplet size are satisfactory for both models
 346 with the second one having a slightly higher evaporation rate at the beginning and lower at
 347 subsequent times. In both cases the droplet's size regression deviates significantly from the d^2 -
 348 law due to the intense and long droplet heat-up period. During this period, the thermal
 349 expansion of the droplet is more intense compared to the droplet evaporation and the droplet
 350 size slightly increases; this phenomenon has been observed in [39, 69] among others. Regarding
 351 the model predictions for the droplet temperature, the available experimental data for the droplet
 352 temperature were obtained by placing three thermocouples at fixed positions ($r/R_0=0, \pm 0.6$).
 353 Such information was difficult to be obtained with the current numerical setup since the droplet
 354 moves over the suspender and also deforms. So, in Fig. 8 the model prediction for the mean
 355 droplet temperature is presented, which is closely related to the measured quantities. The
 356 temperature prediction is in accordance with the experimental measurements but this time the
 357 simplified Fick's model of eq (8) has a better performance predicting accurately the wet-bulb
 358 temperature. The present results are within the accuracy of the results obtained with other
 359 numerical methodologies mentioned at the beginning of this section. It has to be noted that at
 360 the latter stages of evaporation, the interface diffusion problems associated with the VOF
 361 methodology become more pronounced and are more intense for high evaporation rates; this
 362 explains why the droplet temperature predicted with equation (9) further increases for $t > 2.5$ sec.

363



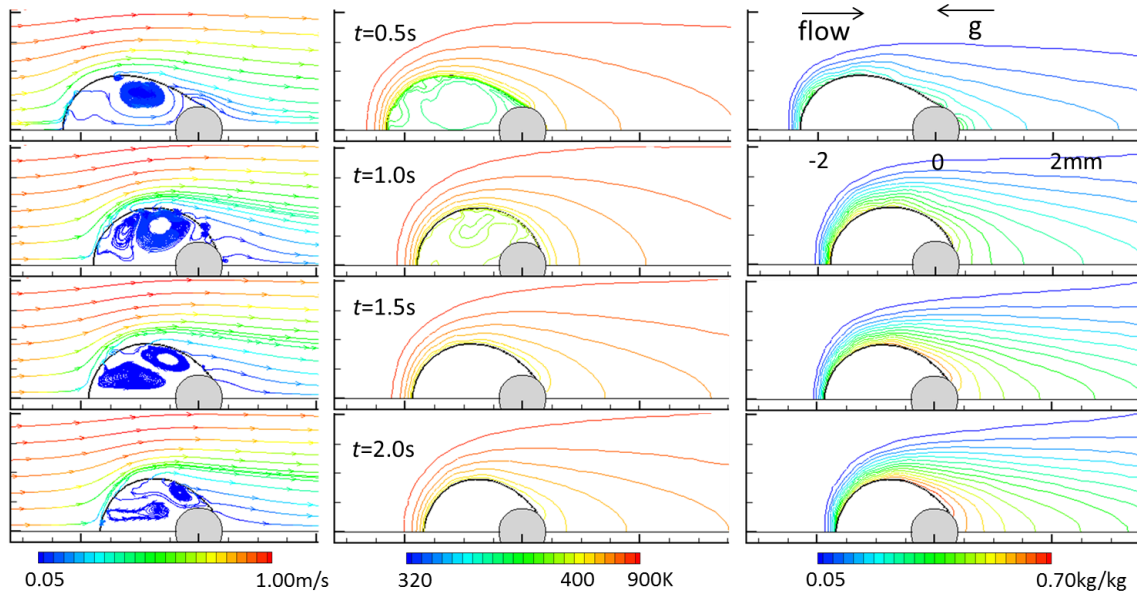
364

365 Fig. 8: Model predictions for the experimental data of Wong & Lin [60]. (a) temporal evolution
366 of droplet size and (b) mean droplet temperature.
367

368 The predicted flow, temperature and vapor concentration field for the experimental case of [60]
369 are shown in Fig. 9. The gravitational forces are quite strong and the droplet moves downwards
370 to the direction of gravity. Since the Re number of the flow is below 20, there is no recirculation
371 in the gas phase downwind the droplet and the temperature and vapor concentration fields have
372 a slightly different topology compared to the cases 1-3 presented in the previous section 4.1.
373 Furthermore, the thickness of the temperature and concentration boundary layers seem to be
374 higher compared to those of cases 1-3 and this ought to the fact that the boundary layer
375 thickness is proportional to $(RePr)^{-1/2}$ [70] as also to the thickening of the boundary layer due to
376 the intense evaporation rate [19].

377 Inside the droplet, the liquid circulation is quite disturbed forming two unsteady vortices which
378 tend to homogenize the temperature. This is in contradiction with the experimental observations
379 of Wong & Lin [60] as also with the numerical solution of Megaridis [30]. The inability to
380 capture this phenomenon in the current work is probably ought to the parasitic velocities
381 induced by the VOF methodology [71, 72], which originate from the imbalance between surface
382 tension and pressure gradient forces. The case examined has a low Re number and the parasitic
383 velocities become important while they are further magnified due to the high density ratio
384 between the liquid and the gas phase, which exceeds 2000 in this case. Nevertheless, the overall
385 behavior of droplet evaporation is not affected by the spurious currents and the experimental
386 data are correctly predicted. In an effort to reduce the magnitude of these velocities, several
387 options were examined, such as reducing the computational time-step down to a Courant
388 number of 0.1, increasing the smoothing iterations of VOF function and using different
389 discretization schemes for the VOF; however, none of these methods could improve the
390 predicted velocity field. The unphysical velocities could be potentially minimized by applying
391 the algorithm described in Francois et al. [72], but the pressure-velocity coupling in FLUENT is
392 hardcoded and cannot be modified as stated in [73]. The CSS surface tension scheme was also
393 examined, but the induced thermo-capillary flow along with the spurious velocities resulted in
394 high deformation of the droplet shape. Thus, the CSS simulations are not considered accurate
395 and they are not presented.

396



397

398 Fig. 9: Predicted flow field streamlines, temperature and vapor concentration field for the
 399 experimental case of Wong & Lin [60].
 400

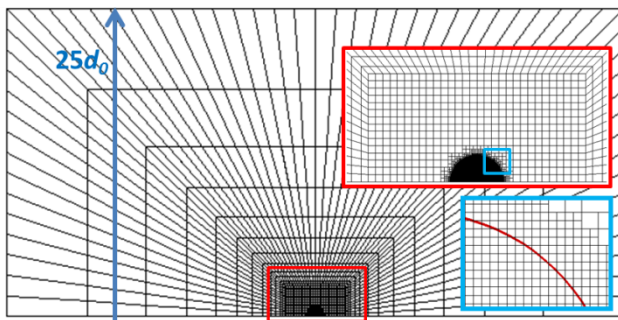
401

402 **4.3 Evaporation at high temperature conditions. Experimental data of Nomura** 403 **et al. [61]**

404 Cases 5-8 of Table 1 correspond to the experimental data of Nomura et al. [61], who examined
 405 the evaporation of suspended n-heptane droplets for a wide range of ambient temperature and
 406 pressure conditions; these data have been widely used to validate 0-D and 1-D models (see [18,
 407 39] among others). The experiments were conducted at microgravity conditions to prevent the
 408 natural convection and the vapor was flowing radially as stated in Nomura et al. [61]. The
 409 droplet diameters examined were in the range 0.6-0.8mm but the exact values were not reported.
 410 However, as the time axis of their plots was presented as t/d_0^2 this normalization results to the
 411 prediction of vaporization time independent on the selection of the droplet diameter. In the
 412 present work, a diameter of 0.7mm was selected as the mean among the experimental values.
 413 Regarding the initial droplet temperature, a value of 300K was used. Simulations of the cases of
 414 [61] were simplified by disabling the solution of the flow equations and accounting only for the
 415 transient and the diffusion terms in the conservation equations. This selection is justified by the
 416 fact that the velocities are quite low and the vapor flows radially [61]. Note that this is not
 417 equivalent to a 1-D model which assumes spherical symmetry, since a 2-D computation domain
 418 is used (Fig. 10) and the grid cells are not aligned with the liquid-gas interface (see inset figure
 419 in Fig. 10). More importantly, the gas phase temperature and concentration are also solved, so
 420 there is no need to estimate “film” gas properties near the interface, as also the Nusselt and

421 Sherwood numbers are not a-priori assumed, but become a part of the solution through the
 422 predicted temperature and vapor concentration gradients. It has also to be noted that this
 423 approach is not applicable in the experiments examined in the previous sections, since the gas
 424 phase velocity plays a dominant role. The grid used is shown in Fig. 10 and it represents an
 425 adiabatic box extended $25d_0$ far from the droplet. The box dimensions are large enough so that
 426 the average gas temperature remains practically constant.

427



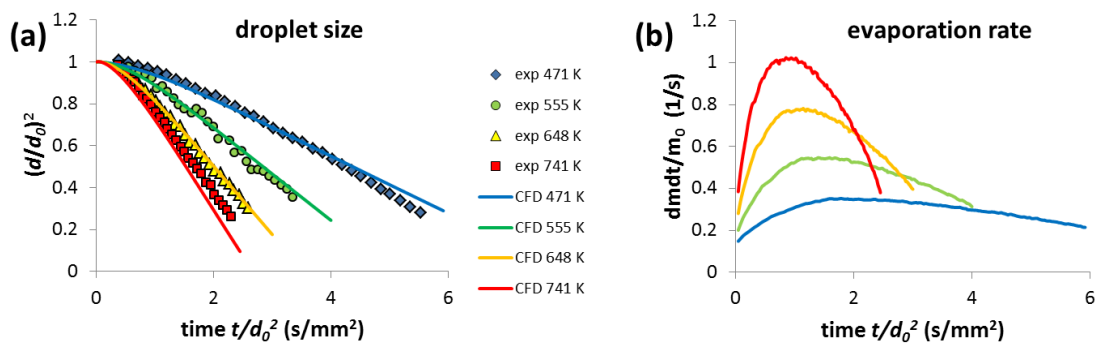
428

429 Fig. 10: Numerical grid used for the experimental data of Nomura et al. [61].

430

431 The model results for the dimensionless squared droplet diameter are shown in Fig. 11a for the
 432 four different ambient temperatures examined. As it can be seen, the model results are
 433 satisfactory for a wide range of ambient temperatures even above the critical one
 434 ($T_{cr,C7}=540.2K$). The droplet evaporation rate is shown in Fig. 11b. The evaporation rate
 435 increases at the initial stages of the evaporation due to droplet heat up and after reaching a
 436 maximum it decreases due to the reduction of the droplet surface area. This behavior is observed
 437 in all cases and it generally increases with increasing ambient temperature.

438



439

440 Fig. 11: Model predictions for the experimental data of Nomura et al. [61]. (a) temporal
 441 evolution of droplet size and (b) evaporation rate.

442

443

444 **5 CONCLUSIONS**

445 The Navier-Stokes equations coupled with the conservation equations for energy and species
446 concentration and the VOF methodology were used to study the evaporation of suspended
447 single- and multi-component droplets. The local evaporation rate was estimated by using the
448 Fick's diffusion law, which is independent of the interface shape and grid density. The model
449 performance was assessed by comparing the results against experimental data for single- and bi-
450 component fuel droplets under sub- and super-critical ambient temperature conditions.
451 Prediction of the overall evaporation rate for a wide range of cases was satisfactory, while
452 prediction of the droplet's temperature was within the accuracy of other published works. For
453 the cases with Re of $O(100)$ the recirculation zones at the gas and the liquid phase are correctly
454 predicted and agree with the numerical solutions from other researchers. For the case with Re of
455 $O(10)$, the model could not capture the liquid phase internal recirculation zone since the
456 parasitic velocities induced by the VOF methodology were large compared to the flow velocity.
457 Overall, the numerical model can be considered as a reliable tool able to predict the lifetime and
458 temporal evolution of droplet evaporation in a wide range of ambient temperature conditions for
459 moderate and high Re numbers. In comparison to simplified (but also faster) 0-D and 1-D
460 models, the present model gives insight into the spatial distribution of the flow variables and
461 more importantly, it can be extended without any modification to predict the evaporation of
462 deformed droplets and droplets undergoing breakup; see [74]. Nevertheless, with the today's
463 computational resources, the present model cannot be used to simulate sprays comprised by a
464 large number of droplets.

465

466 **6 ACKNOWLEDGEMENTS**

467 The research leading to these results has received funding from the People Programme (Marie
468 Curie Actions) of the European Union's Seventh Framework Programme FP7-PEOPLE-2012-
469 IEF under REA grant Agreement No. 329116.

470

471 **7 NOMENCLATURE**

472

Symbol	Quantity	SI Unit
A	Surface area	m^2
B_M	Spalding number $B_M = (Y_{g,sat} - Y_{g,\infty}) / (1 - Y_{g,sat})$	-
c_p	Specific heat capacity	$J/(kg \cdot K)$
d	Diameter	m
\vec{d}	Vector connecting adjacent cells	m
D	Mass diffusion coefficient	m^2/s
E	Specific internal energy	J/kg
F	Force	N
g	Gravity acceleration	m/s^2
h	Specific enthalpy	J/kg
\mathbf{I}	Unit tensor	-
$\vec{J}_{q,k}$	Species flux	kg/m^2s
k	Thermal conductivity coefficient	$W/(m \cdot K)$
L	Latent heat of vaporization	J/kg
\dot{m}''	Evaporation rate	kg/m^2s
\dot{m}'''	Evaporation source term	kg/m^3s
n	Normal coordinate to gas-liquid interface	-
N_{ph}	Total number of phases	-
N_{sp}	Total number of liquid species	-
p	Pressure	N/m^2

Pr	Prandtl number	-
R	Radius	m
r	Coordinate in radial direction	m
Re	Reynolds number $Re = \rho_{g,\infty} d_0 u_\infty / \mu_{g,\infty}$	-
S	Source term	
T	Temperature	K
t	Time	s
u	Velocity	m/s
V	Volume	m ³
x,y,z	Coordinates	m
Y	Mass concentration	kg/kg

473

474 **Greek Symbols**

Symbol	Quantity	SI Unit
α	Liquid volume fraction	-
κ	Curvature	m ⁻¹
μ	Viscosity	kg/(m·s)
ρ	Density	kg/m ³
σ	Surface tension coefficient	N/m

475

476 **Subscripts**

Symbol	Quantity
0	Initial
∞	Conditions far from the droplet

<i>cell</i>	Cell
<i>cr</i>	Critical
<i>d</i>	Droplet
<i>evap</i>	Evaporation
<i>exp</i>	Experimental
<i>g</i>	Gas phase
<i>k</i>	k^{th} species of the mixture
<i>l</i>	Liquid phase
<i>m</i>	Mixture
<i>mean</i>	Mean
<i>q</i>	of phase q
<i>sat</i>	Saturated
<i>surf</i>	Surface interface
<i>vap</i>	Vapor

477

478 **abbreviations**

C10	n-decane
C7	n-heptane
CSF	Continuum Surface Force
CSS	Continuum Surface Stress
ECM	Effective Conductivity Model
FCM	Finite Conductivity Model
FDM	Finite Diffusivity Model
ICM	Infinite Conductivity Model

IDM Infinite Diffusivity Model

VOF Volume Of Fluid

479

480

481 **8 REFERENCES**

482

483 [1] Clift R., Grace J.R., Weber M.E., Bubbles, drops and particles, Academic Press, New York,
484 1978.

485 [2] Sirignano W.A., Fluid Dynamics and Transport of Droplets and Sprays, Cambridge
486 University Press, 1999.

487 [3] Bird R.B., Stewart W.E., Lightfoot E.N., Transport Phenomena, 2nd ed., Wiley, New York,
488 2002.

489 [4] Asano K., Mass Transfer – from Fundamentals to Modern Industrial Applications, Wiley
490 VCH Verlag GmbH & Co. KGaA, Weinheim, Germany, 2006.

491 [5] Givler S.D., Abraham J., Supercritical droplet vaporization and combustion studies, Progress
492 in Energy and Combustion Science, 22 (1996) 1-28.

493 [6] Bellan J., Supercritical (and subcritical) fluid behavior and modeling: drops, streams, shear
494 and mixing layers, jets and sprays, Progress in Energy and Combustion Science, 26 (2000) 329-
495 366.

496 [7] Sazhin S.S., Advanced models of fuel droplet heating and evaporation, Progress in Energy
497 and Combustion Science, 32 (2006) 162-214.

498 [8] Erbil H.Y., Evaporation of pure liquid sessile and spherical suspended drops: A review,
499 Advances in Colloid and Interface Science, 170 (2012) 67-86.

500 [9] Godsave G.A.E., Burning of Fuel Droplets in: 4th International Symposium on combustion,
501 The Combustion Institute, Baltimore, 1953, pp. 818-830.

502 [10] Spalding D.B., The combustion of liquid fuels, in: 4th International Symposium on
503 combustion, The Combustion Institute, Baltimore, 1953, pp. 847-864.

- 504 [11] Law C.K., Unsteady droplet combustion with droplet heating, *Combustion and Flame*, 26
505 (1976) 17-22.
- 506 [12] Law C.K., Sirignano W.A., Unsteady droplet combustion with droplet heating--II:
507 Conduction limit, *Combustion and Flame*, 28 (1977) 175-186.
- 508 [13] Abramzon B., Sirignano W.A., Droplet vaporization model for spray combustion
509 calculations, *International Journal of Heat and Mass Transfer*, 32 (1989) 1605-1618.
- 510 [14] Dombrovsky L.A., Sazhin S.S., A parabolic temperature profile model for heating of
511 droplets, *Journal of Heat Transfer*, 125 (2003) 535-537.
- 512 [15] Yao G.F., Abdel-Khalik S.I., Ghiaasiaan S.M., An Investigation of Simple Evaporation
513 Models Used in Spray Simulations, *Journal of Heat Transfer*, 125 (2003) 179-182.
- 514 [16] Miller R.S., Harstad K., Bellan J., Evaluation of equilibrium and non-equilibrium
515 evaporation models for many-droplet gas-liquid flow simulations, *International Journal of*
516 *Multiphase Flow*, 24 (1998) 1025-1055.
- 517 [17] Kolaitis D.I., Founti M.A., A comparative study of numerical models for Eulerian-
518 Lagrangian simulations of turbulent evaporating sprays, *International Journal of Heat and Fluid*
519 *Flow*, 27 (2006) 424-435.
- 520 [18] Sazhin S.S., Kristyadi T., Abdelghaffar W.A., Heikal M.R., Models for fuel droplet heating
521 and evaporation: Comparative analysis, *Fuel*, 85 (2006) 1613-1630.
- 522 [19] Zhifu Z., Guoxiang W., Bin C., Liejin G., Yueshe W., Evaluation of Evaporation Models
523 for Single Moving Droplet with a High Evaporation Rate, *Powder Technology*, 240 (2013) 95-
524 102.
- 525 [20] Law C.K., Multicomponent droplet combustion with rapid internal mixing, *Combustion*
526 *and Flame*, 26 (1976) 219-233.
- 527 [21] Renksizbulut M., Bussmann M., Li X., Droplet vaporization model for spray calculations,
528 *Particle & Particle Systems Characterization*, 9 (1992) 59-65.
- 529 [22] Varanasi K.K., Clack H.L., Miller R.S., On preferential diffusion of binary component
530 liquid droplets evaporating in a two-phase mixing layer, *International Journal of Multiphase*
531 *Flow*, 30 (2004) 1235-1257.

- 532 [23] Law C.K., Internal boiling and superheating in vaporizing multicomponent droplets,
533 AIChE Journal, 24 (1978) 626-632.
- 534 [24] Kneer R., Schneider M., Noll B., Wittig S., Diffusion controlled evaporation of a
535 multicomponent droplet: theoretical studies on the importance of variable liquid properties,
536 International Journal of Heat and Mass Transfer, 36 (1993) 2403-2415.
- 537 [25] Torres D.J., O'Rourke P.J., Amsden A.A., Efficient multicomponent fuel algorithm,
538 Combustion Theory and Modelling, 7 (2003) 67-86.
- 539 [26] Brenn G., Concentration fields in evaporating droplets, International Journal of Heat and
540 Mass Transfer, 48 (2005) 395-402.
- 541 [27] Renksizbulut M., Haywood R.J., Transient droplet evaporation with variable properties and
542 internal circulation at intermediate Reynolds numbers, International Journal of Multiphase
543 Flow, 14 (1988) 189-202.
- 544 [28] Haywood R.J., Nafziger R., Renksizbulut M., Detailed examination of gas and liquid phase
545 transient processes in convective droplet evaporation, Journal of Heat Transfer, 111 (1989) 495-
546 502.
- 547 [29] Chiang C.H., Raju M.S., Sirignano W.A., Numerical analysis of convecting, vaporizing
548 fuel droplet with variable properties, International Journal of Heat and Mass Transfer, 35 (1992)
549 1307-1324.
- 550 [30] Megaridis C.M., Comparison between experimental measurements and numerical
551 predictions of internal temperature distributions of a droplet vaporizing under high-temperature
552 convective conditions, Combustion and Flame, 93 (1993) 287-302.
- 553 [31] Shih A.T., Megaridis C.M., Suspended droplet evaporation modeling in a laminar
554 convective environment, Combustion and Flame, 102 (1995) 256-270.
- 555 [32] Shih A.T., Megaridis C.M., Thermocapillary flow effects on convective droplet
556 evaporation, International Journal of Heat and Mass Transfer, 39 (1996) 247-257.
- 557 [33] Abou Al-Sood M.M., Birouk M., A numerical study of the effect of turbulence on mass
558 transfer from a single fuel droplet evaporating in a hot convective flow, International Journal of
559 Thermal Sciences, 46 (2007) 779-789.

- 560 [34] Raghuram S., Raghavan V., Pope D.N., Gogos G., Two-phase modeling of evaporation
561 characteristics of blended methanol–ethanol droplets, *International Journal of Multiphase Flow*,
562 52 (2013) 46-59.
- 563 [35] Megaridis C.M., Sirignano W.A., Numerical modeling of a vaporizing multicomponent
564 droplet, *Symposium (International) on Combustion*, 23 (1990) 1413-1421.
- 565 [36] Megaridis C.M., Sirignano W.A., Multicomponent droplet vaporization in a laminar
566 convective environment, *Combustion science and technology*, 87 (1992) 27-44.
- 567 [37] Megaridis C.M., Liquid-Phase Variable Property Effects in Multicomponent Droplet
568 Convective Evaporation, *Combustion Science and Technology*, 92 (1993) 291 - 311.
- 569 [38] Renksizbulut M., Bussmann M., Multicomponent droplet evaporation at intermediate
570 Reynolds numbers, *International Journal of Heat and Mass Transfer*, 36 (1993) 2827-2835.
- 571 [39] Zhang H., Evaporation of a suspended droplet in forced convective high-pressure
572 environments, *Combustion Science and Technology*, 175 (2003) 2237-2268.
- 573 [40] Haywood R.J., Renksizbulut M., Raithby G.D., Transient deformation and evaporation of
574 droplets at intermediate Reynolds numbers, *International Journal of Heat and Mass Transfer*, 37
575 (1994) 1401-1409.
- 576 [41] Schlottke J., Weigand B., Direct numerical simulation of evaporating droplets, *Journal of*
577 *Computational Physics*, 227 (2008) 5215-5237.
- 578 [42] Strotos G., Gavaises M., Theodorakakos A., Bergeles G., Numerical investigation of the
579 evaporation of two-component droplets, *Fuel*, 90 (2011) 1492-1507.
- 580 [43] Banerjee R., Numerical investigation of evaporation of a single ethanol/iso-octane droplet,
581 *Fuel*, 107 (2013) 724-739.
- 582 [44] Ghata N., Shaw B.D., Computational modeling of the effects of support fibers on
583 evaporation of fiber-supported droplets in reduced gravity, *International Journal of Heat and*
584 *Mass Transfer*, 77 (2014) 22-36.
- 585 [45] Malgarinos I., Nikolopoulos N., Marengo M., Antonini C., Gavaises M., VOF simulations
586 of the contact angle dynamics during the drop spreading: Standard models and a new wetting
587 force model, *Advances in Colloid and Interface Science*, 212 (2014) 1-20.

588 [46] Malgarinos I., Nikolopoulos N., Gavaises M., Coupling a local adaptive grid refinement
589 technique with an interface sharpening scheme for the simulation of two-phase flow and free-
590 surface flows using VOF methodology, *Journal of Computational Physics*, 300 (2015) 732-753.

591 [47] Strotos G., Malgarinos I., Nikolopoulos N., Papadopoulos K., Theodorakakos A., Gavaises
592 M., Performance of VOF methodology in predicting the deformation and breakup of
593 impulsively accelerated droplets in: 13th ICLASS, Tainan, Taiwan, 2015.

594 [48] Hirt C.W., Nichols B.D., Volume of Fluid (Vof) Method for the Dynamics of Free
595 Boundaries, *Journal of Computational Physics*, 39 (1981) 201-225.

596 [49] Brackbill J.U., Kothe D.B., Zemach C., A continuum method for modeling surface tension,
597 *Journal of Computational Physics*, 100 (1992) 335-354.

598 [50] Lafaurie B., Nardone C., Scardovelli R., Zaleski S., Zanetti G., Modelling Merging and
599 Fragmentation in Multiphase Flows with SURFER, *Journal of Computational Physics*, 113
600 (1994) 134-147.

601 [51] Perry R.H., Green D.W., Perry's Chemical Engineers' Handbook, 7th ed., McGraw-Hill,
602 1997.

603 [52] Poling B.E., Prausnitz J.M., O'Connell J.P., Properties of Gases and Liquids (5th Edition),
604 in, McGraw-Hill, 2001.

605 [53] Youngs D.L., Time-Dependent Multi-Material Flow with Large Fluid Distortion, in:
606 Morton K.W., Baines M.J. (Eds.) Numerical Methods for Fluid Dynamics,, Academic Press,
607 New York, 1982.

608 [54] Barth T., Jespersen D., The design and application of upwind schemes on unstructured
609 meshes, in: 27th Aerospace Sciences Meeting, American Institute of Aeronautics and
610 Astronautics, 1989.

611 [55] ANSYS®FLUENT, Release 14.5, Theory Guide, in, 2012.

612 [56] Issa R.I., Solution of implicitly discretised fluid flow equations by operator-splitting,
613 *Journal of Computational Physics*, 62 (1986) 40-65.

614 [57] Hu H., Larson R.G., Evaporation of a sessile droplet on a substrate, *Journal of Physical
615 Chemistry B*, 106 (2002) 1334-1344.

- 616 [58] Mollaret R., Sefiane K., Christy J.R.E., Veyret D., Experimental and numerical
617 investigation of the evaporation into air of a drop on a heated surface, *Chemical Engineering*
618 *Research & Design*, 82 (2004) 471-480.
- 619 [59] Daïf A., Bouaziz M., Chesneau X., Ali Cherif A., Comparison of multicomponent fuel
620 droplet vaporization experiments in forced convection with the Sirignano model, *Experimental*
621 *Thermal and Fluid Science*, 18 (1999) 282-290.
- 622 [60] Wong S.C., Lin A.C., Internal temperature distributions of droplets vaporizing in high-
623 temperature convective flows, *Journal of Fluid Mechanics*, 237 (1992) 671-687.
- 624 [61] Nomura H., Ujiie Y., Rath H.J., Sato J.I., Kono M., Experimental study on high-pressure
625 droplet evaporation using microgravity conditions, in: *Symposium (International) on*
626 *Combustion*, 1996, pp. 1267-1273.
- 627 [62] Theodorakakos A., Bergeles G., Simulation of sharp gas-liquid interface using VOF
628 method and adaptive grid local refinement around the interface, *International Journal for*
629 *Numerical Methods in Fluids*, 45 (2004) 421-439.
- 630 [63] Zeng Y., Lee C.F., A model for multicomponent spray vaporization in a high-pressure and
631 high-temperature environment, *Journal of Engineering for Gas Turbines and Power*, 124 (2002)
632 717-724.
- 633 [64] Ozturk A., Cetegen B.M., Modeling of plasma assisted formation of precipitates in
634 zirconium containing liquid precursor droplets, *Materials Science and Engineering A*, 384
635 (2004) 331-351.
- 636 [65] Strotos G., Gavaises M., Theodorakakos A., Bergeles G., Evaporation of a suspended
637 multicomponent droplet under convective conditions, in: *ICHMT, Marrakech, Morocco, 2008*.
- 638 [66] Taneda S., Experimental Investigation of the Wake behind a Sphere at Low Reynolds
639 Numbers, *J. Phys. Soc. Japan*, 11 (1956) 1104-1108.
- 640 [67] Amani E., Nobari M.R.H., A calibrated evaporation model for the numerical study of
641 evaporation delay in liquid fuel sprays, *International Journal of Heat and Mass Transfer*, 56
642 (2013) 45-58.
- 643 [68] Tonini S., Cossali G.E., A novel vaporisation model for a single-component drop in high
644 temperature air streams, *International Journal of Thermal Sciences*, 75 (2014) 194-203.

- 645 [69] Abramzon B., Sazhin S., Convective vaporization of a fuel droplet with thermal radiation
646 absorption, *Fuel*, 85 (2006) 32-46.
- 647 [70] Feng Z.-G., Michaelides E.E., Heat and mass transfer coefficients of viscous spheres,
648 *International journal of heat and mass transfer*, 44 (2001) 4445-4454.
- 649 [71] Harvie D.J.E., Davidson M.R., Rudman M., An analysis of parasitic current generation in
650 *Volume of Fluid simulations*, *Applied Mathematical Modelling*, 30 (2006) 1056-1066.
- 651 [72] Francois M.M., Cummins S.J., Dendy E.D., Kothe D.B., Sicilian J.M., Williams M.W., A
652 balanced-force algorithm for continuous and sharp interfacial surface tension models within a
653 volume tracking framework, *Journal of Computational Physics*, 213 (2006) 141-173.
- 654 [73] Bohacek J., Surface Tension Model for High Viscosity Ratios Implemented in VOF Model,
655 in: *ILASS - Europe*, Brno, Czech Republic, 2010.
- 656 [74] Strotos G., Malgarinos I., Nikolopoulos N., Gavaises M., Numerical investigation of
657 aerodynamic droplet breakup in a high temperature gas environment, *Fuel*, 181 (2016) 450-462.
- 658
- 659